# The Application of the Factorization Method to the Subsurface Imaging of Surface-Breaking Cracks

Chao Zhang, Peter Huthwaite, and Michael Lowe

*Abstract*—A common location for cracks to appear is at the surface of a component; at the near surface, many nondestructive evaluation techniques are available to inspect for these, but at the far surface this is much more challenging. Ultrasonic imaging is proposed to enable far surface defect detection, location, and characterization. One specific challenge here is the presence of a strong reflection from the backwall, which can often mask the relatively small response from a defect. In this paper, the factorization method (FM) is explored for the application of subsurface imaging of the surface-breaking cracks. In this application, the component has two parallel surfaces, the crack is initiated from the far side and the phased array is attached on the near side. Ideally, the pure scattered field from a defect is needed for the correct estimation of the scatterer through the FM algorithm. However, the presence of the backwall will introduce a strong specular reflection into the measured data which should be removed before applying the FM algorithm. A novel subtraction method was developed to remove the backwall reflection. The performance of the FM algorithm and this subtraction method were tested with the simulated and experimental data. The experimental results showed a good consistency with the simulated results. It is shown that the FM algorithm can generate high-quality images to provide a good detection of the crack and an accurate sizing of the crack length. The subtraction method was able to provide a good backwall reflection removal in the case of small cracks (1–3 wavelengths).

*Index Terms*—Backwall subtraction, crack sizing, factorization method (FM), phased array imaging.

## I. Introduction

**D**RIVEN by safety and economic interests, industry sectors including nuclear power generation and aerospace are seeking more accurate technologies for sizing surface-breaking cracks. This is because the length of the crack is the main input in fracture mechanics to calculate the remaining safe life of a component. With a more accurate sizing of the crack, the industries can obtain more accurate life estimates for a component, which can help them to achieve a more cost-efficient schedule for replacing structural components. Generally, the crucial parts, which need accurate nondestructive evaluation (NDE) to size the depth of the crack, include

nozzles, piping components, and vessel welds [1]. These components will have liquid or gas with high temperature and pressure inside during operation. As a result, if surface-breaking cracks exist at the internal surface, it is normally only possible to attach the transducers to the remote side to conduct subsurface detection and sizing of the surface-breaking cracks.

Among the established NDE techniques, there are only two practical modalities for this challenge in subsurface NDE inspections, ultrasonic, and radiography [2]. Radiography is an NDE technique based on measuring X-ray radiation having been transmitted through a component, effectively recording the cumulative attenuation experienced along each ray path. This can provide an indication of any subsurface defects. Because of the principle of this technique, any defect must be well aligned with the ray paths for maximum detectability, and thus a thin crack with unfavorable orientation will be hard to be detected through radiography [3]. Another big issue of radiography is the use of ionizing radiation, which is harmful to humans even in small doses. For the purposes of safety, a large exclusion zone must be cordoned off around the inspection location to prevent any significant human exposure [4]. Compared to radiography, ultrasonic testing is more suitable for routine detection of near backwall surface-breaking cracks as it is safer and much easier to be implemented [5]. A direct idea of sizing the surface-breaking crack in ultrasonic testing is to measure the flight time of the diffracted echoes and calculate the crack depth with the knowledge of the geometry of the component, which has led to the development of the impulse-echo technique (IET) and the time-of-flight diffraction technique (TOFD). Her and Lin [6], [7] applied the IET to conduct the through-wall detection of the surface-breaking cracks, while Baby *et al.* [8] evaluated the depth of the surface-breaking crack on the far surface using the TOFD. The results of their work showed that these methods can achieve a good accuracy for a crack larger than one wavelength but have a poor performance for the cracks smaller than one wavelength [6], [8].

Ultrasonic phased array imaging is an alternative for the reliable sizing of the near backwall surface-breaking cracks [9]. The approach is as follows. First, the full matrix capture (FMC) is acquired; in this, each transducer transmits a signal in turn, which is then measured by all of the transducers in the array. Ultimately, this produces a set of signals for all send-receive combinations in the array, giving a complete data set of the scattering problem. From this data set, it is possible to perform a number of different imaging

algorithms to generate an image of the area under inspection as a postprocessing stage. The total focusing method (TFM) is one of the most widely used postprocessing methods and is implemented by focusing a sound beam to each point in the region of interest and assessing the reflections from these points [10]. As the standard TFM only considers the direct ray path of the ultrasound, it is not developed for near backwall defects, where there is additional complexity from the wave reflecting from the backwall. In response, Felice *et al.* [11] developed the half-skip TFM (HSTFM) to measure the depth of the surface-breaking crack that is near the backwall. The results showed that the HSTFM has the ability to size a 1.5-wavelength surface-breaking crack that is impossible to be measured through the conventional TFM; however, the HSTFM still had a poor accuracy for the cracks smaller than 1.5 wavelength [12]. As the TFM and the HSTFM are based on the weak scattering approximation (e.g., the Born approximation), there is a resolution limit called the Rayleigh limit (0.5 wavelength) that will limit the application of these methods in high-resolution imaging [13].

Qualitative inverse scattering methods, which were developed recently, are also postprocessing techniques that can be used for ultrasonic phased array imaging [13]. The approach is a noniterative method for obstacle reconstruction with the knowledge of the measured data of the far/near scattered field. The qualitative methods do not resort to the weak scattering approximation (i.e., Born approximation) and are established to reconstruct the shape of the inhomogeneities inside the material rather than the quantitative values of the object function. The recent development in the qualitative method has led to the establishment of the factorization method (FM) by Kirsch and Grinberg [14]. Since being established, the FM has attracted much research consideration and has already been successfully applied to different inverse scattering problems [15]–[17]. Recently, the application of the FM in ultrasonic testing to achieve super-resolution imaging (i.e., beyond the Rayleigh limit) has become a focus. For example, Simonetti [18] has proved that the linear sampling method (LSM) and FM can achieve a super-resolution imaging, and the feasibility of the super-resolution was validated through a limited view experiment performed on a metallic plate. A similar result was obtained in [19] that the FM is able to achieve a resolution better than the Rayleigh limit in the application of ultrasonic phased array imaging. Because of the attractive potential of the FM in defect detection and shape construction, we have attempted to use the FM in the problem of the subsurface imaging of surface-breaking cracks. As mentioned before, only one side (near side) is accessible in the situation of subsurface imaging and the back wall of the component can be regarded as a strong reflector that would bring strong specular reflection. A practical consideration of applying the FM for subsurface imaging is that the FM ideally requires the data of the scattered field purely from the defect itself, rather than the total field (i.e., including the backwall), but the measured field of a phased array is always the total field. As the scattered signal is weak compared to the incident wave and the specular reflection, the imaging result will be strongly influenced by the incident wave and

specular reflection. As a result, in order to ensure an accurate image of the scatterer, we must extract the scattered field from the recorded signal. To solve this problem, we have proposed a method that extracts the scattered field from the measured data captured on a component containing the defect. In some cases [12], the removal of the specular component is achieved by angling the incoming beam such that the specular reflection does not return to the array. The issue is that this generally requires the use of wedges, restricts the illumination angle, and makes longer path lengths, increasing attenuation, and therefore, this approach is not pursued in this paper.

The remainder of this paper is organized as follows. First, we introduce the formulation of the inverse scattering problem, briefly review the FM, and introduce the classical implementation of the FM in Section II. In Section III, the subtraction method, which removes the incident wave and specular reflection, is introduced in detail. Then, the results based on the simulated data are shown, and the effectiveness of the FM is discussed in Section IV. In Section V, the experimental data were captured through the FMC and processed by the subtraction method, which is described in Section III to extract the scattered field, then the results based on the TFM and FM are compared. Finally, we provide the conclusion in Section VI.

## II. BACKGROUND THEORY

### A. Direct Scattering

The direct scattering problem is that of calculating the scattered field when an incident field interacts with the scatterers, according to the physical properties of scatterers and physical model. The formulation here is based on [20] and considers the acoustic equations in 2-D. In the frequency domain, the propagation of a time harmonic acoustic wave with a wavenumber $k > 0$ is governed by the Helmholtz equation

$$\Delta u + k^2 u = 0 \tag{1}$$

where $u$ is the scalar field potential. We define an object function in $\mathbb{R}^2$ as

$$O(\mathbf{r}) = \left[ \left( \frac{c_0}{c(\mathbf{r})} \right)^2 - 1 \right] \tag{2}$$

where $c(\mathbf{r})$ is the sound speed at a point $\mathbf{r}$ and $c_0$ is sound speed in the background. We define $\bar{D} \subset \mathbb{R}^2$ as the support of the object function, and $\bar{D}$ has a smooth boundary $\partial D$. We consider a planar incident wave with an incident direction $\hat{\mathbf{r}}_0$

$$u_i = e^{ik\hat{\mathbf{r}}_0 \cdot \mathbf{r}} \tag{3}$$

where $\hat{\mathbf{r}}_0 = (\mathbf{r}_0 / |\mathbf{r}_0|)$. This denotes a planar wave field at point $\mathbf{r}$ due to an illumination from the direction $\mathbf{r_0}$. Taking the object function into account, we derive the solution of this 2-D scattering problem

$$(\Delta + k^2)u(\mathbf{r}) = -Ou(\mathbf{r}) \tag{4}$$

$$u = e^{ik\hat{\mathbf{r}}_0 \cdot \mathbf{r}} + u_s \tag{5}$$

where $u_s$ represents the scattered field. For the scattered field, the Sommerfeld radiation condition should be satisfied to ensure that all energy is radiated outward toward infinity

$$\lim_{r \to \infty} \sqrt{r} \left( \frac{\partial u_s}{\partial r} - i k u_s \right) = 0 \quad \text{for } r = |\boldsymbol{r}|. \tag{6}$$

Also, the Sommerfeld radiation condition must be understood to hold uniformly in all directions. It has been proven in [21] that solving (4) and (5) is a well-posed problem. As a result of the Sommerfeld radiation condition, for large $|r|$, the scattered field $u_s$ can be asymptotically formed in the expansion

$$u_s(\boldsymbol{r}) = \frac{e^{ikr}}{\sqrt{r}} u_\infty(\hat{\boldsymbol{r}}) + \mathcal{O}\left(r^{-\frac{3}{2}}\right) \tag{7}$$

where $\hat{\boldsymbol{r}}$ is the observation direction and $u_\infty(\hat{\boldsymbol{r}})$ is the far-field pattern of the scattered field. It has already been proven [22] that solving (2)–(6) is equivalent to solving the Lippmann–Schwinger integral equation

$$u(\boldsymbol{r}, \hat{\boldsymbol{r}}_0) = e^{ik\hat{\boldsymbol{r}}_0 \cdot \boldsymbol{r}} - k^2 \int_D O(\boldsymbol{r}') u(\boldsymbol{r}', \hat{\boldsymbol{r}}_0) G(\boldsymbol{r}, \boldsymbol{r}') d\boldsymbol{r}'. \tag{8}$$

The $G(\boldsymbol{r}, \boldsymbol{r}')$ in (8) is the free space Green's function that is used to describe how a wave field propagates from an excitation point $\boldsymbol{r}$ to an observation point $\boldsymbol{r}'$. In 2-D, the $G(\boldsymbol{r}, \boldsymbol{r}')$ is given as

$$G(\boldsymbol{r}, \boldsymbol{r}') = -\frac{i}{4} H_0^{(1)}(k|\boldsymbol{r} - \boldsymbol{r}'|) \tag{9}$$

where $|\boldsymbol{r} - \boldsymbol{r}'|$ is the distance between the measurement point and the excitation point, and $H_0^{(1)}$ is a zero-order Hankel function of the first kind. As $|\boldsymbol{r} - \boldsymbol{r}'| \to \infty$, the $G(\boldsymbol{r}, \boldsymbol{r}')$ has the asymptotic form in 2-D

$$G_\infty = -\frac{e^{i\left(\frac{\pi}{4} + kr\right)}}{\sqrt{8\pi k r}} e^{-ik\boldsymbol{r} \cdot \boldsymbol{r}'}. \tag{10}$$

Equation (8) indicates the dependence of the total field on the incident field and its own value within $D$. The integration of the total field in (8) makes the forward scattering problem to be nonlinear. For the far-field ($r \to \infty$), (8) can be written as

$$u(\boldsymbol{r}, \hat{\boldsymbol{r}}_0) = e^{ik\hat{\boldsymbol{r}}_0 \cdot \boldsymbol{r}} + \Pi f(\hat{\boldsymbol{r}}, \hat{\boldsymbol{r}}_0) \frac{e^{ikr}}{\sqrt{r}} \tag{11}$$

where

$$\Pi = \frac{k^2 e^{\frac{i\pi}{4}}}{\sqrt{8\pi k_0}} \tag{12}$$

$$f(\hat{\boldsymbol{r}}, \hat{\boldsymbol{r}}_0) = \int_D O(\boldsymbol{r}') u(\boldsymbol{r}', \hat{\boldsymbol{r}}_0) e^{-ik\hat{\boldsymbol{r}} \cdot \boldsymbol{r}'} d\boldsymbol{r}'. \tag{13}$$

The term $f(k_0\hat{\boldsymbol{r}}, k_0\hat{\boldsymbol{r}}_0)$ refers to the scattering amplitude in some of the literature [13]. Equations (5) and (7)–(10) lead to

$$u_s(\hat{\boldsymbol{r}}) = -k^2 \int_D O(\boldsymbol{r}') u(\boldsymbol{r}', \hat{\boldsymbol{r}}_0) G(\hat{\boldsymbol{r}}, \boldsymbol{r}') d\boldsymbol{r}' \tag{14}$$

$$u_\infty(\hat{\boldsymbol{r}}) = -k^2 \frac{e^{i\pi/4}}{\sqrt{8\pi k_0}} \int_D O(\boldsymbol{r}') u(\boldsymbol{r}', \hat{\boldsymbol{r}}_0) e^{-ik\hat{\boldsymbol{r}} \cdot \boldsymbol{r}'} d\boldsymbol{r}'. \tag{15}$$

Equation (14) implies that the ideal imaging of the scatterers needs the knowledge of the pure scattered field from the scatterers, rather than the total field. In the case of subsurface imaging of the surface-breaking cracks, effectively we want the scattered component from the defect, but not from the backwall; however, in real inspections, it is the total field—which contains the scattered components from the defect and from the backwall—that will be recorded by the phased array. In response, we proposed a method to extract the scattered field from the total field in Section III for the phased array subsurface imaging.

### B. Inverse Scatering

*1) Born Approximation:* The Born approximation is a linear scattering approximation that aims to simplify the scattering problem and makes noniterative imaging possible. It can be used directly for diffraction tomography, and is also implied in other algorithms, such as the TFM. The Born approximation is valid when the medium is weakly scattering, i.e., the size of the object is comparable to the wavelength and the contrast between the background and the inhomogeneities is small. Using the Born approximation is fast and robust for imaging problems, this is because it allows a direct mapping from the scattering amplitude to the spatial Fourier transform of the object function

$$f(\hat{\boldsymbol{r}}, \hat{\boldsymbol{r}}_0) \propto \mathcal{O}(k(\hat{\boldsymbol{r}}_0 - \hat{\boldsymbol{r}})). \tag{16}$$

The right-hand side term of (16) is also called the K space, and the definition of it is given by

$$\mathcal{O}(\boldsymbol{R}) = \mathcal{F}[O](\boldsymbol{r}) \tag{17}$$

where $\mathcal{F}$ means the Fourier transform and $\boldsymbol{R}$ is the spatial frequency. It can be seen from (16) that by varying $\boldsymbol{r}$ and $\hat{\boldsymbol{r}}_0$ around all the possible angles, the value of every spatial frequency in the Ewald disk [13] can be measured. However, the spatial frequency outside the circle (greater than $2k$) cannot be measured; thus, the highest resolution that the imaging methods based on the Born approximation can achieve is ($\lambda/2$).

*2) Factorization Method:* The FM is a recent algorithm for the reconstruction of a scatterer [23]–[25]. It is developed as an alternative to the LSM. Although a comprehensive overview of the LSM is beyond the scope of this paper, a brief introduction of LSM is helpful to understand the FM. To start the derivation of the LSM, we shall first introduce an incident field $v_g$, which is defined as

$$v_g(\boldsymbol{r}) = \int_{\mathbb{S}^2} e^{ik\boldsymbol{r} \cdot \hat{\boldsymbol{r}}_0} g(\hat{\boldsymbol{r}}_0) ds(\hat{\boldsymbol{r}}_0) \tag{18}$$

where $g$ is called the Herglotz density, physically corresponding to the amplitude of plane waves in each direction $\boldsymbol{r}_0$ that are superposed to form the incident field, and $v_g$ is also called the Herglotz wave function. Here, $\mathbb{S}^2$ denotes the unit sphere in $\mathbb{R}^3$. Equation (18) also leads to the definition of the Herglotz operator $H : L^2(\mathbb{S}^2) \to L^2(\partial D)$, given as

$$(Hg)(\boldsymbol{r}) = \int_{\mathbb{S}^2} e^{ik\boldsymbol{r} \cdot \hat{\boldsymbol{r}}_0} g(\hat{\boldsymbol{r}}_0) ds(\hat{\boldsymbol{r}}_0). \tag{19}$$

Then, an operator $F : L^2(\mathbb{S}^2) \to L^2(\mathbb{S}^2)$ based on the far-field pattern $u_\infty$ is denoted by

$$(Fg)(\hat{\boldsymbol{r}}) = \int_{\mathbb{S}^2} u_\infty(\hat{\boldsymbol{r}}, \hat{\boldsymbol{r}}_0) g(\hat{\boldsymbol{r}}_0) ds(\hat{\boldsymbol{r}}_0) \tag{20}$$

where $\hat{r} = (r/|r|)$. Here, $u_\infty(\hat{r}, \hat{r}_0)$ is the far-field pattern of the scattered field for incident plane waves from all possible directions $\hat{r}_0$ and observed at all the possible directions $\hat{r}$. The left-hand term, $Fg$, is actually equivalent to the far-field pattern of the scattered field created by the incident field $v_g$ defined in (18). This compact operator $F$ is of great importance as it forms the basis of the LSM and the FM. For a sampling point at $z \in \Omega$, the far-field operator is defined as

$$Fg_z = \Phi_\infty(\hat{r}, z, k) \tag{21}$$

where $\Phi_\infty$ is the far-field pattern of the Green's function, namely

$$\Phi_\infty(\hat{r}, z, k) = \frac{1}{4\pi} e^{-ik\hat{r}\cdot z}. \tag{22}$$

It has been proven (see [26]) that

$$z \in D \iff \Phi_\infty(\cdot, z, k) \in \mathcal{R}(F) \tag{23}$$

where $\mathcal{R}(F)$ denotes the range of the operator $F$. With these premises, according to [21], the theorem that is usually given to describe the approximate solution of (21) is as follows.

1) If $z \in D$, then for every $\varepsilon > 0$, there exists a solution $g_z^\varepsilon$ that

$$||Fg_z^\varepsilon(\cdot) - \Phi_\infty(\cdot, z, k)||_{L^2(\Omega)} < \varepsilon \tag{24}$$

and

$$\lim_{z \to \partial D} ||g_z^\varepsilon||_{L^2(\Omega)} = \infty \tag{25}$$
$$\lim_{z \to \partial D} ||v_{g_z^\varepsilon}||_{H^1(D)} = \infty \tag{26}$$

where $v_{g_z^\varepsilon}$ is the Herglotz wave function with density $g_z^\varepsilon$.

2) If $z \in \mathbb{R}^2 \backslash \bar{D}$, then for every $\varepsilon > 0$ and $\delta > 0$, there exists a solution $g_z^\varepsilon$ that

$$||Fg_z^{\varepsilon,\delta}(\cdot) - \Phi_\infty(\cdot, z, k)||_{L^2(\Omega)} < \varepsilon + \delta \tag{27}$$

and

$$\lim_{\delta \to 0} ||g_z^{\varepsilon,\delta}||_{L^2(\Omega)} = \infty \tag{28}$$
$$\lim_{\delta \to 0} ||v_{g_z^{\varepsilon,\delta}}||_{H^1(D)} = \infty \tag{29}$$

where $v_{g_z^{\varepsilon,\delta}}$ is the Herglotz wave function with density $g_z^{\varepsilon,\delta}$.

After obtaining the above results, it is clear that the behavior of the $||g_z||_{L^2(\Omega)}$ can be used to reconstruct the support of the object $D$. The common method is to solve the far-field equation $Fg_z = \Phi_\infty(\hat{r}, z, k)$ by applying a proper regularized technique at first, and then, using $\mathcal{I}(z) = 1/||g_z||_{L^2(\Omega)}$ as an indicator function to reconstruct the support of the object $D$.

The LSM offers a noniterative method for fast and accurate reconstruction of the shape of an obstacle. One significant challenge with the LSM is that the regularized results of the far-field equation does not converge when the noise in the data approaches zero. The motivation of the introduction of the FM by Kirsch is to modify the far-field equation to avoid the convergence problem. According to [14], a factorization of the operator $F$ can be derived in the form

$$F = H^*SH \tag{30}$$

where $H$ is the the Herglotz operator, $H^*$ is the adjoint operator of $H$, and $S : L^2(\partial D) \to L^2(\partial D)$ is the interaction operator that transforms the incident field inside the object into a source distribution that characterizes the perturbation to the incident field. This factorization is the basis of the FM and is responsible for its name. Based on this factorization, it has been proven in [26] that instead of interrogating the range of $F$, a higher quality image can be formed by interrogating the range of $H$. In particular, Fioralba and David [27] has demonstrated that the range of $H$ coincides with the range of $(F^*F)^{(1/4)}$. Therefore, the FM replaces the far-field operator $F$ in (21) by the operator $(F^*F)^{(1/4)}$, and then, the far-field equation becomes

$$(F^*F)^{\frac{1}{4}}g = \Phi_\infty. \tag{31}$$

It can be shown that the (31) has a solution if and only if $z \in D$ (see [14] for a detailed derivation). Further, $z \in \mathbb{R}^2$ belongs to $D$ if and only if

$$\sum_{i=1}^\infty \frac{1}{|\sigma_i|} |\langle \Phi_\infty(\hat{r}, z), \psi_i \rangle_{L^2}|^2 < \infty \tag{32}$$

where $\{\sigma_i, \psi_i, \hat{\psi}_i\}_1^\infty$ is the singular system of $F$. Equation (32) is also called the Picard's criterion. By utilizing the behavior of the Picard's criterion, an indicator function can be yielded as

$$\text{FM}(z) = \frac{1}{\sum_{i=1}^\infty \frac{1}{|\sigma_i|} |\langle \Phi_\infty(\hat{r}, z), \psi_i \rangle_{L^2}|^2}. \tag{33}$$

As a result, if a point $z$ belongs to $D$, the value of (33) will be nonzero but will be zero otherwise [14]. After applying the indicator function through the whole grid of the target region, a scalar image can be reconstructed and the object is represented by nonzero points.

In this paper, the FM is implemented in the frequency domain, and the spectral data $F(w)$ of the far-field operator, which is also called the multistatic response matrix, is used for the calculation of the FM. The multistatic response matrix $F(w)$ is actually built from the recorded FMC data using fast Fourier transforms (FFTs) at the angular frequency $w$ [26]. By assuming a linear array containing $N$ elements, the calculation process of the multistatic response matrix in this paper is as follows. First, after the acquisition of the FMC data, an $N \times N$ matrix is provided, whose $(m,n)$th element is actually the recorded time-domain signal from $m$th transmitter to $n$th receiver, where $1 \leqslant m \leqslant N$ and $1 \leqslant n \leqslant N$; then, the FFT of each element in this $N \times N$ matrix is calculated; after that, the complex value of the FFT result at frequency $w$ of $(m,n)$th element is used as the $(m,n)$th entry of the $F(w)$. For other time-domain implementations of the related sampling methods, the reader is referred to [25] and [28]–[30] for details.
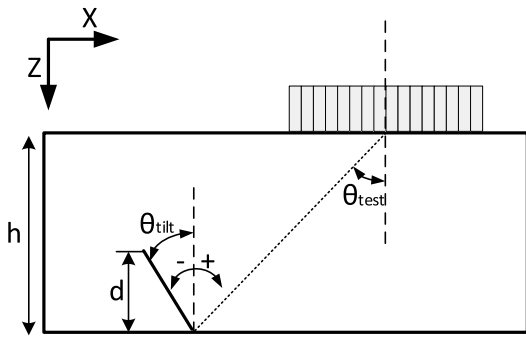
Fig. 1.   Schematic showing the inspection of a sample containing a surface-breaking crack.

## III. ELIMINATING THE INCIDENT WAVE AND THE BACKWALL REFLECTION

### A. Imaging for Surface-Breaking Cracks

In this paper, we focus on the problem of subsurface imaging of the surface-breaking cracks. Consider a sample that has two flat parallel surfaces, a thickness of $h$ and a surface-breaking crack located at the lower surface, as shown in Fig. 1. The array is attached to the remote side to perform the subsurface imaging. The direction that the crack grows out is demonstrated as $\theta_{tilt}$ with the vertical. The depth $d$ of the crack is the vertical distance between the crack tip and the backwall. The line joining the center of the array to the point where the crack connects to the backwall makes an angle of $\theta_{test}$ with the vertical. Thus, the horizontal distance between the point that the crack initiates and the center of the array can be calculated by $h * \tan\theta_{test}$.

Actually, the angle $\theta_{test}$ not only relates to the relative position between the crack and the array, but also to the available viewing aperture. Ideally, the FM needs the measured data of the scattered field of all possible directions of excitation and all possible data of observation, i.e., measurements from a circular array completely surrounding the scatterer. In the case of limited view, according to the work done by Hutt and Simonetti [31], a small reduction in the aperture will dramatically degrade the image reconstructed by the FM. As a result, the first priority for the application of the FM imaging in the case of subsurface imaging is to make the the available viewing aperture as big as possible. In the configuration shown in Fig. 1, the biggest aperture is achieved by setting $\theta_{test}$ to zero. This also has the advantage of minimizing the propagation path length, hence improving the signal strength. However, this brings another big problem for imaging. The backwall of the object can be regarded as a strong reflector that would bring a strong specular reflection. Conventionally, this problem is solved by detecting the crack at an oblique incident angle (e.g., $\theta_{test} = 45°$), and the resulting measured signals will contain only the tip diffraction and the echoes from the root corner since the specular backwall reflection will not be measured by the array [12]. However, with longer propagation distance, there will be greater attenuation, reducing signal-to-noise, and similarly coherent noise from grain scattering will also be worse for longer path lengths. The (often necessary)
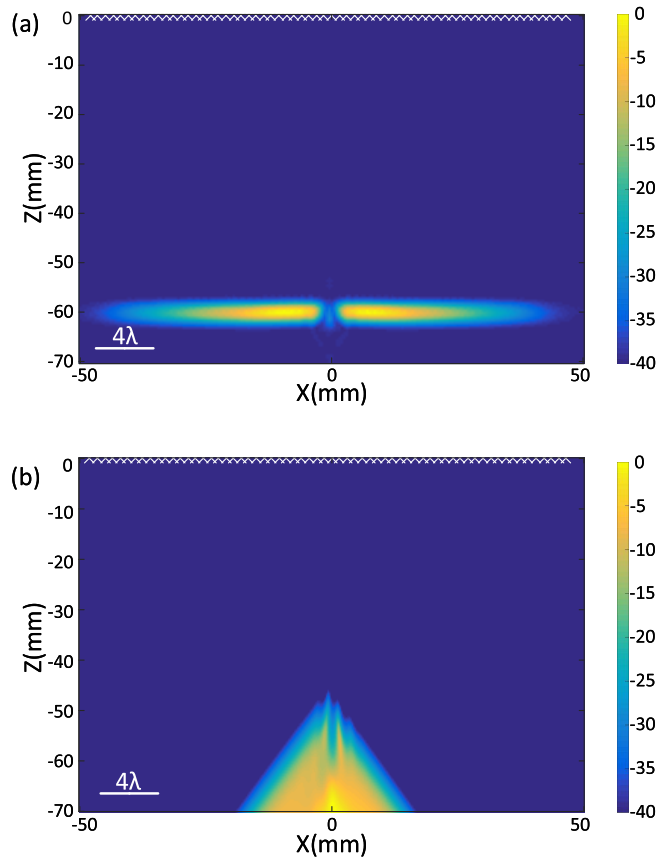


Fig. 2.   (a) TFM and (b) FM images obtained using simulated array data for the configuration in Fig. 1, when $h = 60$ mm, $d = 6$ mm, $\theta_{test} = 0°$, and $\theta_{tilt} = 0°$.

introduction of wedges introduces complexities of its own. In order to ensure the biggest aperture and also improve the signal strength, the zero incident angle ($\theta_{test} = 0°$) is chosen, that means the strong specular reflection will be recorded together with the scattered signals during recording. When a small crack is being detected at $\theta_{test} = 0°$, as the scattered waves from the crack are much weaker than the backwall reflection, the indication of the crack will be totally masked by the strong indications of the backwall and artifacts introduced by the backwall reflection [Fig. 2(a) and (b)].

As a result, when detecting at $\theta_{test} = 0°$, in order to ensure a good imaging result that contains clear indications of the crack, the backwall reflection should be removed from the recorded signal before imaging.

### B. Removing Backwall Reflection From the Measured Data

One possible way of the extracting the scattered field is by measuring the total field of a defect-free copy of the component which contains the defect; this method is referred to as baseline subtraction in this paper. However, this method is not practical in real inspection as it is not possible to achieve a defect-free copy of the component. Another commonly used method is gating, i.e., to calculate the arrival time of the backwall reflection and set the corresponding sections of the measured signals to zero at these locations. Due to the complexity of the elasticity and the geometry, the arrival time
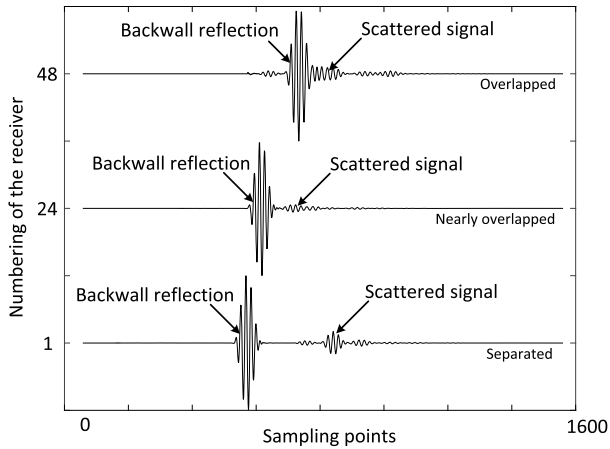
Fig. 3. Time traces of three different elements based on the simulated array data for the configuration in Fig. 1, when $h = 60$ mm, $d = 6$ mm, $\theta_{test} = 0°$, $\theta_{tilt} = 0°$, and the element 1 is used as the transmitter while all the elements used as receivers.

is actually hard to accurately calculate in practical applications and an accurate calculation still needs a defect-free component to calibrate. The main disadvantage of a simple gating is that scattered signals that overlap with the backwall reflection will be lost. In the subsurface imaging of the surface-breaking cracks, the amplitude of the backwall reflection is much larger than the scattered signal and the signals commonly overlap with each other, as shown in Fig. 3. As many imaging algorithms (e.g., FM) are sensitive to the entirety of the scattered field, the loss of information will strongly influence the image result and will typically introduce artifacts or shadows. Thus, gating is not the best solution for the removal of backwall reflection here.

For an array with $N$ elements, after the acquisition of FMC, the recorded data contain $N \times N$ time traces. We denote the measured data with the $i$th element used as transmitter and the $j$th element used as receiver by $I(i, j)$, where $i = 1 \ldots N$ and $j = 1 \ldots N$. We can arrange the measured data into $N$ different series based on $|i - j|$, i.e., the absolute difference between the sender and the receiver element number. Each series$\{k\}$ contains $N - k$ time traces

$$\text{series}\{k\} = \{I(l, l + k), 1 \leq l \leq N - k\}$$
$$\cup \{I(l + k, l), 1 \leq l \leq N - k\} \quad (34)$$

where $k = 0 \ldots N - 1$. By assuming that the upper and lower surfaces of the component are flat and parallel and the material is homogeneous, for the transmitter and receiver pairs with the same $|i - j|$ (element $i$ used as transmitter and element $j$ used as receiver), the ray paths of the backwall reflection will be the same, while the ray paths of the scattered signal will be different [Fig. 4(a)]. In other words, for element pairs of the same lateral separation, the length of ray paths of backwall reflections are identical for the case of two planar surfaces. That means these signals will have the same arrival time and amplitude of the backwall reflection, but different arrival time and amplitude of the scattered signal [Fig. 4(b)].

As the backwall reflection behaves in a well-defined manner, but the signal scattered from the defect is much less

correlated [Fig. 4(b)], the scattered signal can be regarded as the incoherent noise to the backwall reflection for this series of data. As a result, the backwall reflection $B(k)$ for series$\{k\}$ can be estimated

$$B(k) = \frac{1}{2(N - k)} \sum_{i=1}^{N-k} (I(i, i + k) + I(i + k, i)) \quad (35)$$

where $i = 1 \ldots N$ and $k = 0 \ldots N - 1$, i.e., by averaging the matched signals together to minimize the scattered components present. In this paper, if not otherwise specified, the summation and averaging in (35) are implemented over the full time duration. Having obtained the backwall reflection of each series of data, the scattered signal can be extracted by subtracting this estimated backwall reflection from the total field

$$S(i, j) = I(i, j) - B(|i - j|) \quad (36)$$

where $i = 1 \ldots N$ and $j = 1 \ldots N$. This method for removing the backwall reflection works for the components with flat, parallel surfaces, and homogeneous material. In theory, it may be possible to achieve the same approach with more complex geometries, provided that enough averages of each distinct backwall component can be obtained. In practice, it is likely that the case considered here is the only one where this is possible. This method is called the FMC subtraction in this paper. One problem for this method is that with the bigger the $k$ value, the series$\{k\}$ will have fewer time traces, which will influence the averaging in (35). This will result in an inaccurate estimation of the backwall reflection, so some residue of the backwall reflection will remain in $S(i, j)$ after subtraction. Actually, for real inspections, even using baseline subtraction to remove the backwall reflection will introduce some residue as small difference in phase and amplitude will always exist between the measured data. In this paper, we use the method above to extract the scattered signal from the experimentally measured signals.

## IV. IMAGING STUDIES USING FINITE ELEMENT SIMULATIONS

### A. FE Model Description

In this paper, finite element (FE) modeling has been used to compare the performances of the TFM and the FM on imaging the surface-breaking crack and to study the effects of the FMC subtraction mentioned in Section III-B.

Fig. 5 shows a schematic of the FE model used to simulate the phased array imaging of the surface-breaking crack. This model has been run using the commercial FE package ABAQUS/Explict [32]. The input source was introduced by exciting a concentrated force with a time-varying amplitude on the source point. The input force signal was a 5-cycle tone burst with a center frequency of 2 MHz. We have defined 64 source points distributed uniformly on the upper surface to represent a 64-element phased array. Every source point was also set as a monitoring point as every element of a phased array can be used as a transmitter and a receiver. The material used for simulation was steel with a density of 7700 kg/m³, a Young's modulus of 195 GPa, and a Poisson ratio of 0.28.
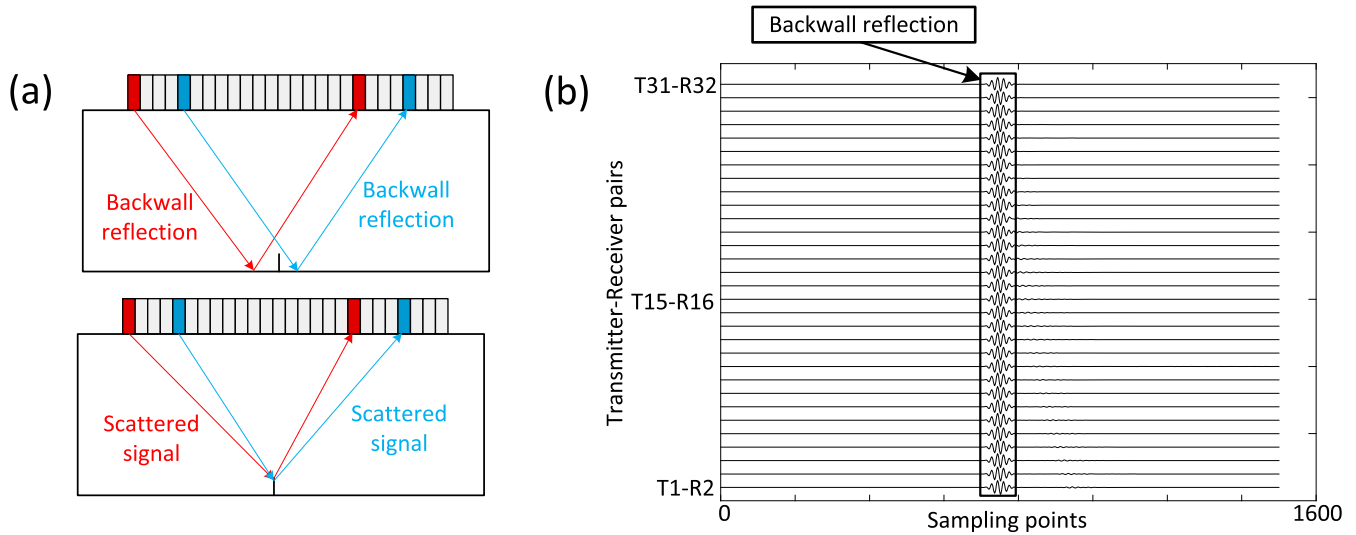
Fig. 4. (a) Schematic showing the components of a received signal. (b) Time traces of different transmitter-receiver pairs with same $|i - j|$ based on the simulated array data for the configuration in Fig. 1, when $h = 60$ mm, $d = 6$ mm, $\theta_{\text{test}} = 0°$, and $\theta_{\text{tilt}} = 0°$.
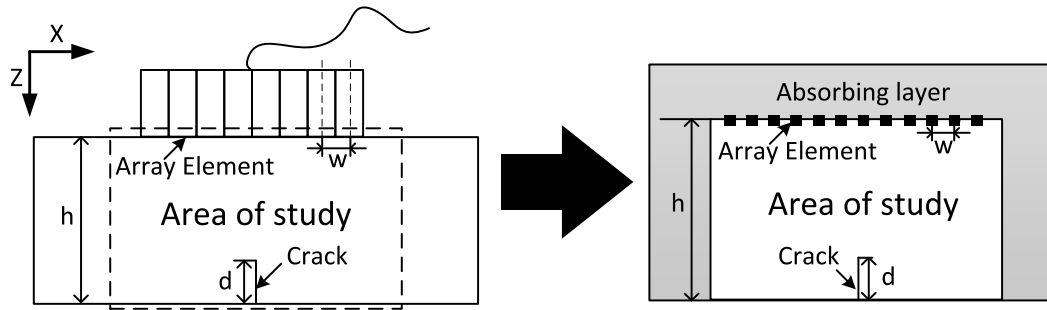


Fig. 5. Schematic of the FE model (not to scale).

Thus, the wavelength $\lambda$ of the longitudinal wave was about 3 mm. To simplify the problem, the material was isotropic throughout. The sample had a thickness of $h = 60$ mm and a surface-breaking crack of $\theta_{\text{tilt}} = 0°$, while the phased array was placed at $\theta_{\text{test}} = 0°$ to ensure the largest angle of view. The four node bilinear plane strain quadrilateral elements with a length of 0.1 mm were utilized in this model. For simplification, only the longitudinal wave was excited and recorded at monitoring points [33]. The shear waves and mode conversions between the longitudinal and shear waves are not considered in this paper, this is because these waves always arrive later than the longitudinal waves used for imaging and the derivation of the FM is based on the acoustic waves which are a type of longitudinal wave. Absorbing layers [34] were attached to the model to absorb any wave entering them, acting as "reflectionless boundaries," to effectively model a small section of an infinite region. In order to simulate the working process of phased array imaging, the 64 source elements were fired successively while all the monitoring points were working simultaneously, which was described as the FMC in Section I. As the purpose of the simulation is to compare the performance of the imaging algorithms and the backwall subtraction methods, the simulation results from different crack depths are necessary. As a result, six models

with the same material and array parameters but different crack depths were created and the crack depths were $0.5\lambda$, $1\lambda$, $2\lambda$, $3\lambda$, $4\lambda$, and $5\lambda$, respectively.

### B. FM Versus TFM

In this section, the performance of the TFM and the FM were compared directly by using them to image the same surface-breaking cracks. For the comparison between the TFM and the FM, the backwall reflections were subtracted using the baseline subtraction as the baseline subtraction is easy to be realized with the numerical data, and will enable the backwall reflections to be removed clearly. In the following numerical examples, if not otherwise specified, the TFM is performed in the time domain, i.e., using the full frequency spectrum of the recorded signals, and the FM is performed using the central frequency component of the recorded signal. In addition, all of the eigenvalues at the central frequency are used to generate the FM images. Thus, the TFM uses all the available information in the signals, while for the FM, some part of the information contained in the measured signals is discarded. Actually, it is still an open question exactly how much more information there is in the full spectrum versus just at a single frequency.
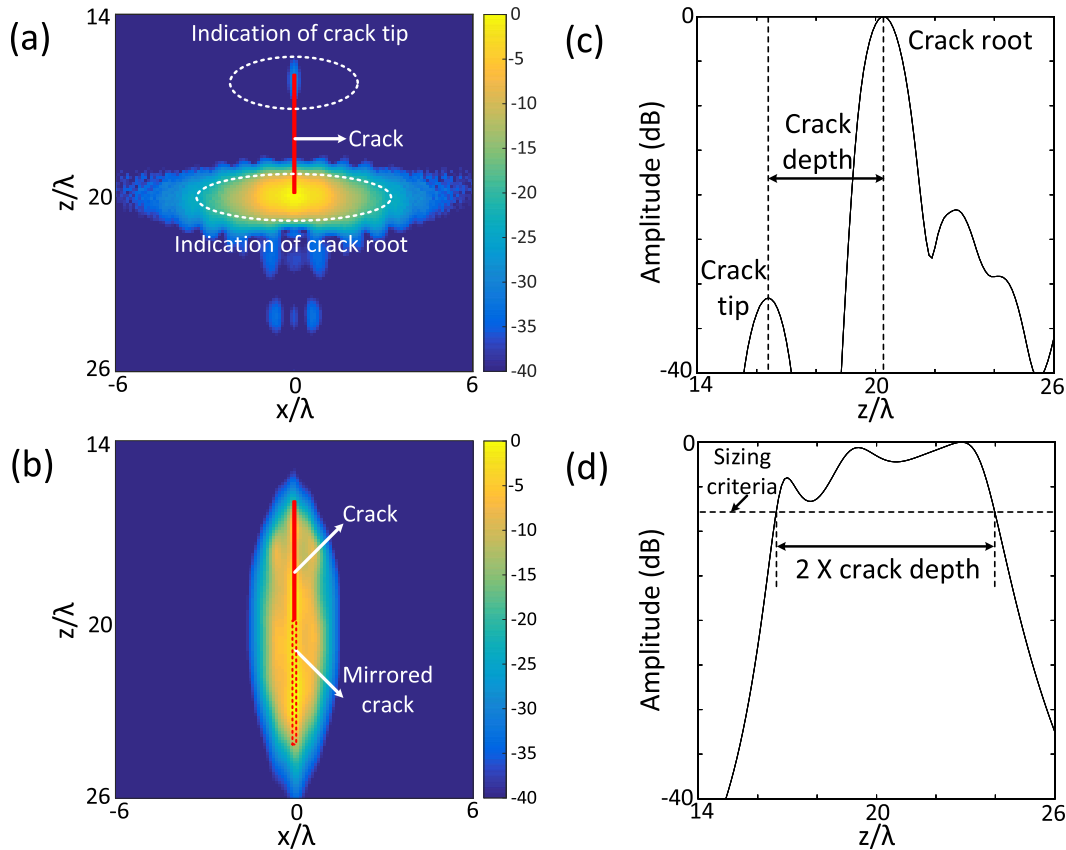
Fig. 6. (a) TFM image of a $4\lambda$ deep crack. (b) FM image of a $4\lambda$ deep crack. (c) Crack sizing method for the TFM image. (d) Crack sizing method for the FM image. Note that the red lines in the images were used to indicate the location and length of the crack in models and the amplitude is on dB scale, normalized to the maximum value in each image. The results here were from the simulated data.

The TFM algorithm and the FM algorithm were applied to the simulated FMC data and the resulting images based on the data from the model with a crack depth of $4\lambda$ are shown in Fig. 6(a) and (b), respectively. From Fig. 6(a), it is clear that the conventional TFM successfully reconstructed the crack tip and the crack root to indicate the presence of the crack. However, the intensity of the indication of the crack tip was much smaller than the indication of the crack root as the energy of the tip diffraction is weak. At the same time, the tip is not as obvious as the root and the intensity of the artifacts in the image are comparable to the crack tip. As a result, if the TFM is used in practical application of imaging surface-braking cracks, the tip indication may not be distinguishable from the artifacts, so the crack will be hard to size. From Fig. 6(b), we can see that both the location and the shape of the crack has been reconstructed correctly by the FM. Because of the advantage in resolution, the image reconstructed by the FM is sharper and clearer than the image reconstructed by TFM, additionally, as the FM attempts to directly reconstruct the shape of the object, the defect in the resulting FM image is easier to identify as a crack than the TFM image.

The principal objective of subsurface imaging is to have an accurate sizing of the surface-breaking crack. As the indications of the crack are different between the TFM image and the FM image, the sizing methods used for the FM image are quite different from the TFM image. For the FM, the sizing method is shown in Fig. 6(d). In this, the center of the crack $x_c$ is determined at the position where the pixel has the maximum amplitude in the image, then the image value at $x = x_c$ is plotted against vertical distance $z$ after that, the $z$ values of the two points on the plot whose amplitude are equal to the sizing criteria are measured, where the sizing criterion is a manually set number used for sizing, e.g., $-6$ dB or $-12$ dB, and finally, the crack depth is equal to half of the difference of the two measured $z$ values, due to the mirroring effect. For the TFM image of the same crack, the image value at the same $x_c$ is plotted, but the crack depth is determined by measuring the distance between the peak of the root indication and the peak of the tip indication [Fig. 6(c)].

In the FM image, it can be noticed that half of the indication of the crack is just above the location of the backwall and half of the indication is beneath the backwall, i.e., the imaging algorithm reconstructed a mirrored crack in the image. That is because for a point $P$ along the crack above the backwall, there are different ray paths of the ultrasound from the transmitter to the point $P$ and back to the receiver. One travels directly from the transmitter to $P$ and back to the receiver, while another one is reflected in the backwall at each interaction. There are also other "half skip" paths which are reflected on the backwall once, either before or after interacting with the
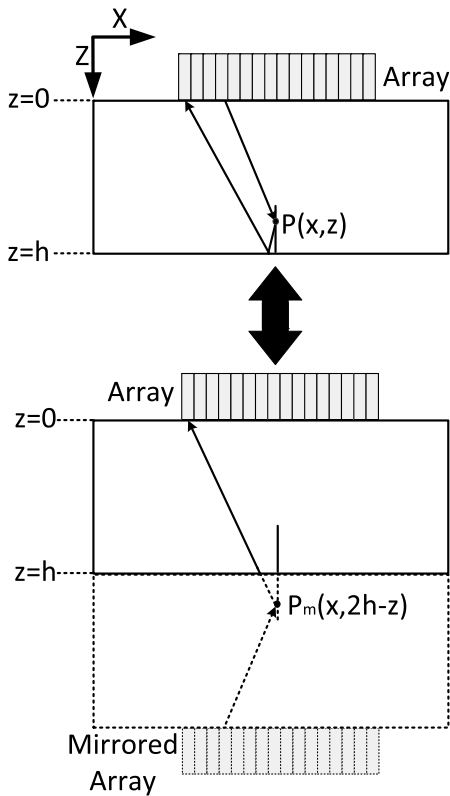
Fig. 7.   Schematic of the wave undergoing the half-skip reflection, which causes mirror effect in the FM images.

defect. The length of the predefect reflection half-skip path is that of a path from the mirrored array to the mirrored point $P_m$ beneath the backwall and then directly back to the real array, as shown in Fig. 7. It is noted that the same is true for a postdefect reflection by reciprocity. For the FM imaging algorithm, when the position of the real array is used for imaging, the ultrasound waves that underwent the direct ray path gave the intensity to the point $P$ above the backwall and the waves that underwent the half-skip reflection gave the intensity of the point $P_m$ beneath the backwall.

The noise and the depth of the crack were not considered in the previous comparison. From (33), we can notice that the FM uses all the eigenvalues including those with very small amplitudes. Those small eigenvalues contain the information of the object and are crucial for achieving super-resolution; however, those eigenvalues are easy to be lost or corrupted with the presence of the noise. The TFM method is essentially a beamforming algorithm that mainly depends on the large eigenvalues [31], i.e., the reason why the TFM is more noise robust than FM. Typically, the imaging algorithms will experience various levels of noise, and will be used with a variety of crack sizes. In order to compare the TFM algorithm and the FM algorithm in a more direct way and explore the limitations of each imaging algorithm, the two algorithms were applied to the simulated data with different crack depths and noise levels, as shown in Fig. 8. Various levels of additive white Gaussian noise were added to the simulated signals. The noise was scaled relative to the root-mean-square (RMS) magnitude

of the simulated signal, e.g., 20-dB SNR corresponds to noise with an RMS magnitude of 10% of the RMS magnitude of the simulated signal. As the TFM is noise robust, only two extreme noise levels (50 and 5 dB) are considered here. For the TFM images, with the smaller crack depth, the indication of the crack tip is closer to the indication of the crack root, as the energy of the tip diffraction is much weaker than the energy reflected by the root corner, the indication of the crack tip is much weaker than the root, which causes the tip to be masked by the root in the TFM image of the $1\lambda$ deep crack. The smallest crack that TFM can successfully reconstruct is about $2\lambda$, which shows good consistency with other research focused on imaging small cracks [12]. The TFM algorithm shows excellent robustness to noise as the addition of the noise does not affect the TFM images. When the backwall reflection is removed clearly, the FM algorithm shows good robustness to the reduction of the crack depth and the addition of the noise, but one trend is also very clear: with an increase in noise, more artifacts are introduced around the reconstructed cracks in the images. As the indication of the crack shape is much more robust than the artifacts introduced by the noise in the FM image, the judgment and sizing of the crack would not be influenced by the addition of the noise when a pure scattered field is used for imaging. The FM has an advantage in imaging resolution [35], and it directly estimates the crack shape rather than estimating the indication of crack tip and root, thus it can reconstruct a small crack that cannot be successfully reconstructed by TFM, e.g., a $1\lambda$ deep crack.

Fig. 9 shows the sizing results of the TFM and the FM methods with different crack depths and noise levels. The TFM shows a very accurate estimation of the crack depth with an error smaller than 5%. The TFM also shows excellent noise robustness as the sizing results stay the same when the noise level varies. However, for the TFM, cracks which are smaller than $2\lambda$ are neither detectable nor measurable. Fig. 9 shows the sizing results of the FM under two different sizing criteria, e.g., $-6$ and $-12$ dB. Using the different sizing criteria, the sizing results of the FM are also different. By using the $-6$ dB as the criterion, the crack depths were undersized; while using the $-12$ dB criterion, the FM is able to accurately size the crack from $1\lambda$ and the sizing results show a good consistency to the sizing results of TFM. For the cracks larger than $1\lambda$, the FM can provide an accurate sizing even for a large noise level (SNR = 5 dB) with an error smaller than 7.5%. The noise level will affect the sizing results of the FM algorithm, especially for the small cracks, as the sizing error for the $1\lambda$ crack is 5% when SNR = 50 dB but 20% when SNR = 5 dB; however, for the cracks larger than $1\lambda$, the influence of the noise level is negligible.

### C. Effect of Subtraction Methods

In this section, the effects of two different methods to remove the backwall reflections to enhance the reconstruction of near-backwall defects are compared. Among the two methods, one is the baseline subtraction and the other one is the FMC subtraction, and the definition for each of these can be found in Section III-B. The removal of the backwall
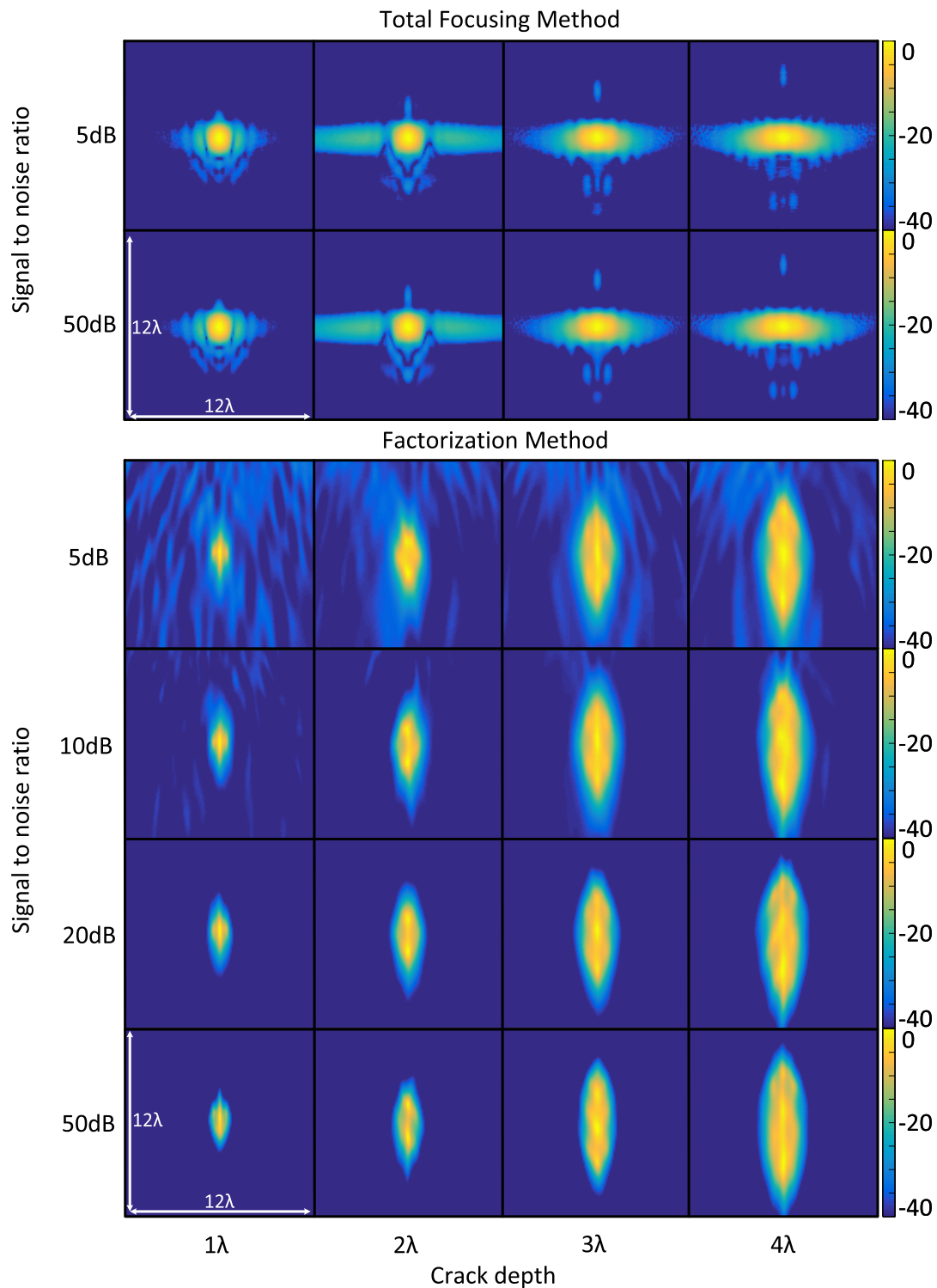
Fig. 8. Imaging results of the TFM and the FM with various noise levels and crack depths. The TFM results contain only two noise levels as the TFM is not sensitive to the noise. Note the images were normalized to the maximum value in each image. The results here were from the simulated data.

reflections of measured data is based on subtraction of the pure backwall reflection when the crack is absent. For the baseline subtraction, the pure backwall reflection is obtained through measuring the data from a defect-free copy of the component under inspection, while for the FMC subtraction, the pure backwall reflection is reconstructed based on the FMC data obtained through the component under inspection. Taking

the simulation model with a crack depth of $2\lambda$ as an instance, we denote the measured data with the $i$th element used as transmitter and the $j$th element used as a receiver by $I(i, j)$, where $i = 1, \ldots, 64$ and $j = 1, \ldots, 64$, then part of the estimated backwall reflections used in the baseline subtraction and the FMC subtraction are plotted in Fig. 10. By observing the plots carefully, we can find that for the FMC subtraction
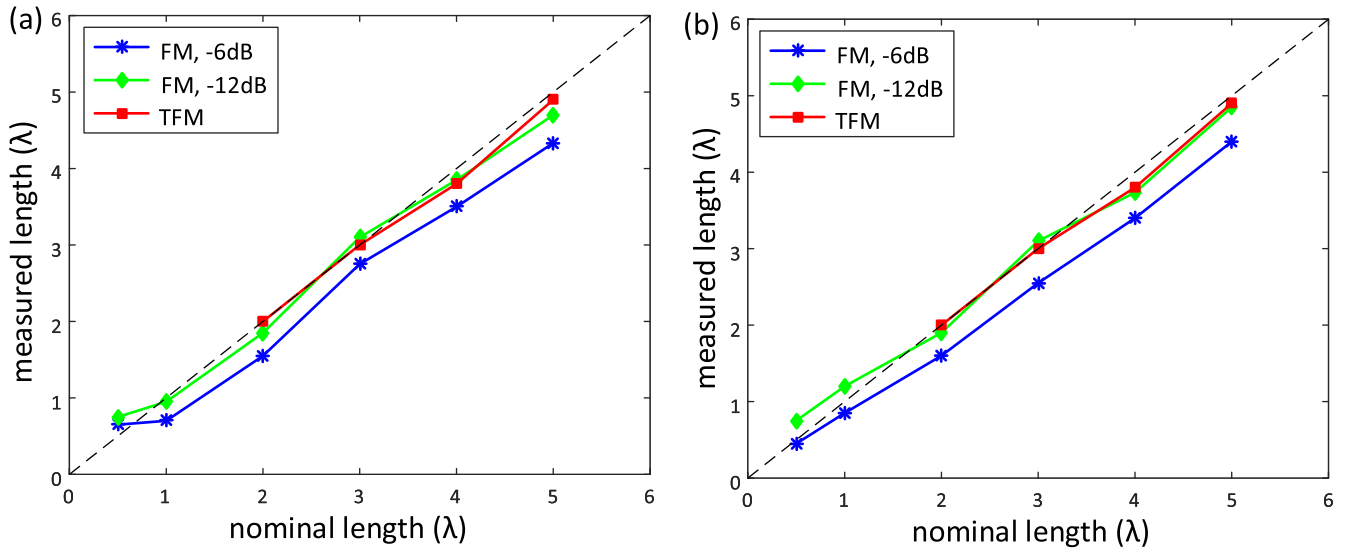
Fig. 9. Sizing results of the TFM and the FM with different crack depths and noise levels. (a) Sizing results when SNR = 50 dB. (b) Sizing results when SNR = 5 dB. The −6 and −12 dB correspond to the amplitudes relative to the peak at which the end of the crack is considered to end, providing a sizing estimate.
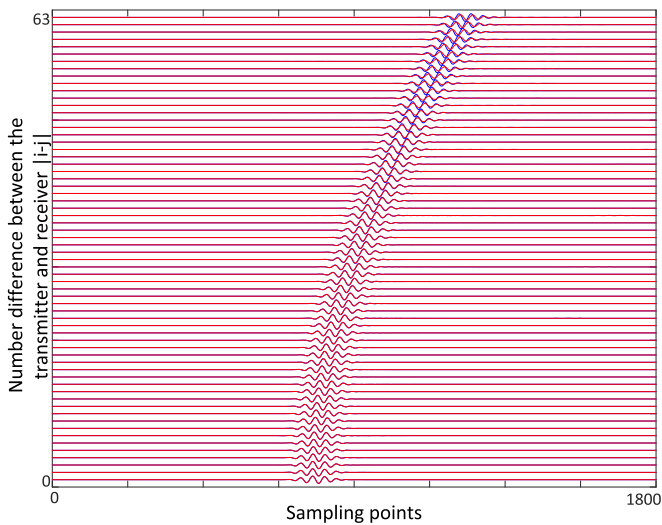


Fig. 10. Plots of the pure backwall reflections used in the baseline subtraction (blue) and the FMC subtraction (red). Note that the array element 1 is used as the transmitter, while all the elements used as receivers.

method, the reconstructed pure backwall reflections are quite close to the pure backwall reflection obtained through the defect-free model, especially when the number difference between the transmitter and the receiver, i.e., $|i - j|$, is small. With the $|i - j|$ becoming larger, the FMC subtraction starts to underestimate the amplitude of the pure backwall reflection although the phases are correctly estimated. This is because the reconstruction of the backwall reflection from the FMC data based on the averaging of different time traces with the same $|i - j|$, and for large $|i - j|$ there are fewer time traces in the FMC data compared to the small $|i - j|$. As an example, for $|i - j| = 1$, there are 126 time traces in FMC data, e.g., $I(1, 2), I(2, 1), \ldots, I(63, 64), I(64, 63)$. However,

for $|i - j| = 63$, there are only two time traces contained in the FMC data: $I(1, 64)$ and $I(64, 1)$. As a result, with large $|i - j|$, there are only a few time traces that can be used for averaging, then the backwall reflection estimate is likely to be of limited accuracy. For all of the estimated backwall reflections obtained by 35, the biggest error is 45% and the smallest error is 1.8% when compared to the backwall reflection used in the baseline subtraction. Because of the presence of the errors, there are some residual components of backwall reflection after FMC subtraction, which will influence the quality of the images generated. As the error varies for different time traces and there are huge numbers of time traces contained in the FMC data, it is hard to study the effects of the FMC subtraction directly. A possible way is to compare the imaging results using different subtraction methods.

Fig. 11(a) is the TFM image of a $2\lambda$ crack without removing the backwall reflection. This image contains a very strong indication of the backwall which masks the indication of the crack root. As a result, it is hard to judge the type of the defect, thus the sizing of the crack will be impossible. Fig. 11(b) is the TFM image after the backwall reflection was clearly removed by the baseline subtraction. This image shows a clear indication of the crack root and the crack tip, and according to Section IV-B, will provide an accurate estimation of the crack depth. Fig. 11(c) is the TFM image after the backwall reflection was removed by the FMC subtraction. This image provides a good indication of the crack root and crack tip and is quite close to Fig. 11(b). It indicates that the FMC subtraction can remove the most part of the backwall reflection and the effect of this method is roughly equal to the baseline subtraction for the TFM algorithm. Additionally, the FMC subtraction also showed good noise robustness for the TFM algorithm as the TFM images were generated at a high noise level, i.e., SNR = 5 dB. It should be noted that FMC subtraction approach suppresses the backwall more effectively
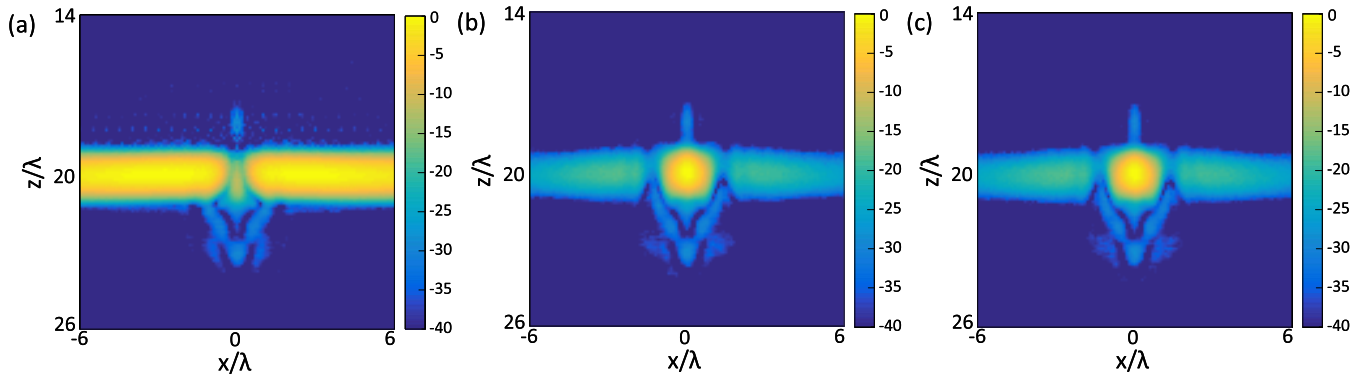
Fig. 11.    TFM images of a $2\lambda$ crack when SNR $=$ 5 dB. (a) Without removing the backwall reflection. (b) Backwall reflection was removed by baseline subtraction. (c) Backwall reflection was removed by FMC subtraction. Note that the images were normalized to the maximum value in each image. The results here were from the simulated data.
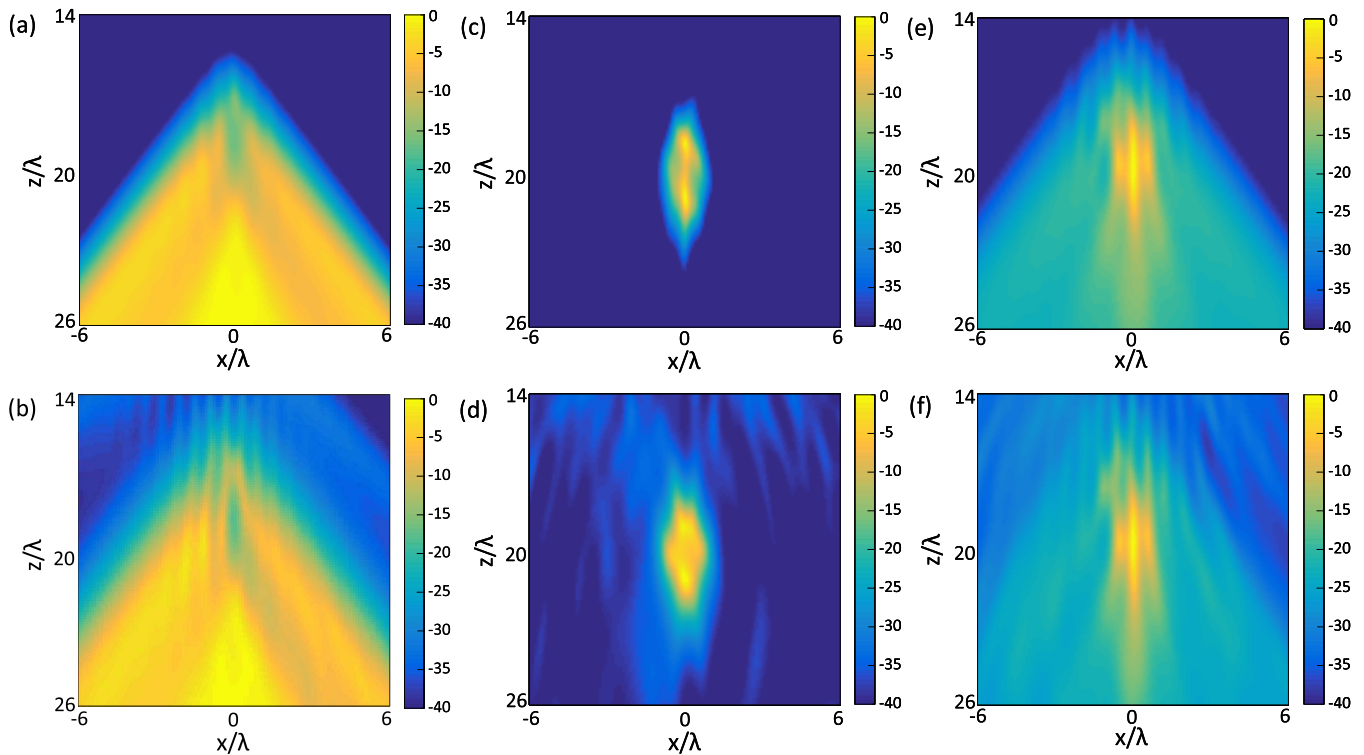


Fig. 12.    FM images of a $2\lambda$ crack. (a) Without removing the backwall reflection at SNR $=$ 50 dB. (b) Without removing the backwall reflection at SNR $=$ 5 dB. (c) Backwall reflection was removed by baseline subtraction at SNR $=$ 50 dB. (d) Backwall reflection was removed by baseline subtraction at SNR $=$ 5 dB. (e) Backwall reflection was removed by FMC subtraction at SNR $=$ 50 dB. (f) Backwall reflection was removed by FMC subtraction at SNR $=$ 5 dB. Note that the images were normalized to the maximum value in each image. The results here were from simulated data.

away from the defect location, since the defect itself can introduce some coherent components that are not removed by averaging.

Fig. 12(a) and (b) shows a $2\lambda$ crack without removing the backwall reflection at SNR $=$ 50 dB and SNR $=$ 5 dB, respectively. From these two images, we can see that the strong indication introduced by the backwall reflection totally masked the indication of the crack. Fig. 12(c) and (d) shows the FM images of a $2\lambda$ crack with baseline subtraction at SNR $=$ 50 dB and SNR $=$ 5 dB, respectively. It is clear that the removal of the backwall reflection can significantly improve the quality of the FM images, both in the defect

judgment and crack sizing. Additionally, after the baseline subtraction, the FM gave good noise robustness as when the noise level became larger, the indication of the crack kept sharp and stable. Fig. 12(e) and (f) shows the FM images of a $2\lambda$ crack with FMC subtraction at SNR $=$ 50 dB and SNR $=$ 5 dB, respectively. These two images have a sharp indication of the crack that indicates that the FMC subtraction has removed the most part of the backwall reflection. However, as the FM algorithm is much more sensitive to noise than the TFM algorithm, the effect of the residual backwall reflection after the FMC subtraction becomes much more obvious. This component introduced strong artifacts into the FM images,
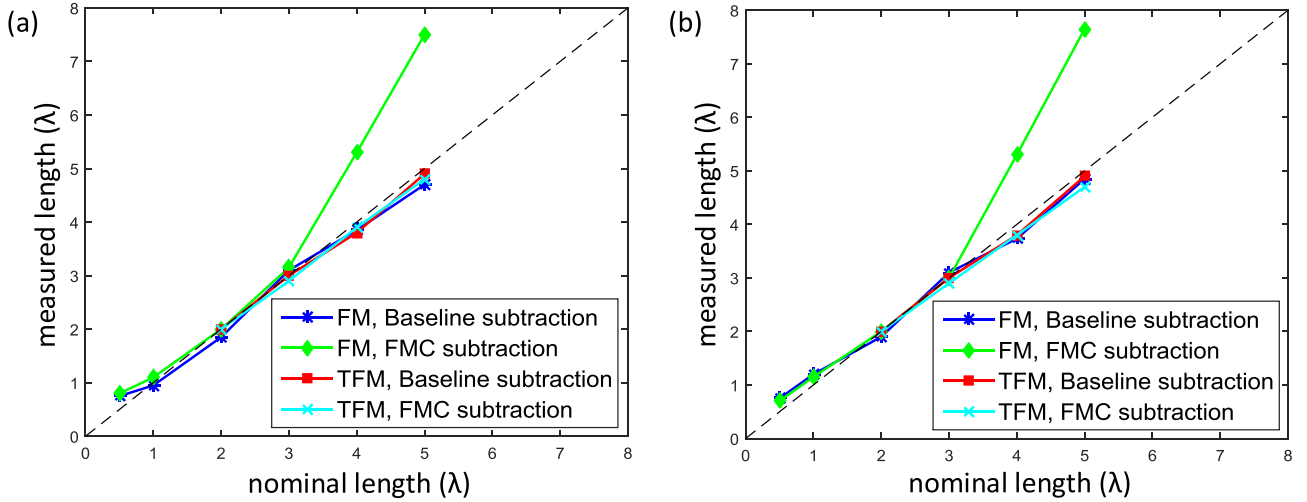
Fig. 13. Sizing results of the FM images and the TFM images using different methods to remove the backwall reflection. (a) Sizing results when SNR = 50 dB. (b) Sizing results when SNR = 5 dB.

which are the strong side bars near the indication of the crack. These artifacts raise the risk of falsely judging the type of the defect. However, these two images also showed good robustness to the noise as the indications of the crack remained stable and sharp even at a high noise level. Except for the image quality, the effects of the FMC subtraction on the sizing accuracy should also be studied, as one of the main objectives of imaging is to provide an accurate sizing. Fig. 13 shows the sizing results of the TFM images and the FM images using different methods to remove the backwall reflection. From these sizing results, we can see that by using the FMC subtraction to remove the backwall reflection, the FM algorithm is able to provide an accurate sizing for a crack whose depth is between $1\lambda$ to $3\lambda$, which means that the FMC subtraction only works for small cracks. This is because the primary assumption of the FMC subtraction is that the amplitude of the scattered signal is much smaller than the backwall reflection, when the crack becomes larger, the assumption become invalid. However, given that the goal is to improve imaging and sizing of the smallest defects, this trend is not entirely problematic. For the sizing results of the TFM images, it is clear that the effect of the FMC subtraction is roughly equal to the baseline subtraction as the sizing results based on these two methods are quite close to each other.

## V. EXPERIMENT RESULTS

For the experimental validation, two arrays with center frequencies of 1 and 5 MHz were used. These two array probes were manufactured by IMASONIC ($Haute-Sa\hat{o}ne$, France), the details of the parameters are shown in Table I. A mild steel sample with a thickness of 38 mm was used (ultrasonic longitudinal wave velocity = 5960 m/s). This sample contains an electrical discharge machining (EDM) notch whose depth is 11 mm and width is 0.5 mm. As a result, for the 1-MHz probe, the notch is $1.85\lambda$ and for the 5-MHz probe, the notch is $9.23\lambda$. The FMC data were collected from this sample using two different probes listed in Table I, with the same array configuration of $\theta_{\text{test}} = 0$ (Fig. 1). After the acquisition

TABLE I
ARRAY PARAMETERS

| Array parameter | Probe 1 | Probe 2 |
|---|---|---|
| Element number | 64 | 64 |
| Element width (mm) | 1.6 | 0.5 |
| Element pitch (mm) | 2.1 | 0.6 |
| Centre frequency (MHz) | 1 | 5 |
| Bandwidth (-6dB; MHz) | 0.756 to 1.33 | 3.37 to 6.64 |

of the FMC data, the backwall reflections were removed by the FMC subtraction. For generating the experimental images, the TFM was performed in the time domain, while the FM was performed at the central frequency of the array probe and used all the eigenvalues at the central frequency to generate images, which is in accordance with our numerical simulations. The central frequencies and bandwidths of the two array probes used for experimental validation are listed in Table I. The TFM and the FM imaging results at different frequencies are shown in Fig. 14. These image results based on the experimental data show a good consistency with the imaging results based on the simulations. Fig. 14(a) and (b) are the FM images of the 11-mm EDM at different center frequencies. These two images give us a very good indication of the EDM notch; however, there are also some strong artifacts, i.e., the "side bars" near the main indication, which were in consistent with our numerical examples [see Fig. 12(e) and (f)] and were considered to be introduced by using the FMC subtraction to remove the backwall reflection. Fig. 14(c) and (d) shows the TFM images based on the experiment data acquired by two different array probes. It can be seen from the Fig. 14(c) that the amplitude of the artifacts introduced by the noise is comparable to the tip indication, which makes the judgment and the sizing of the notch difficult if the real location and shape of the defect is unknown in advance. The sizing results from these images were shown in Table II.

From the sizing results, we can see that the FM algorithm gives us a good estimation of the crack depth at 1 MHz but failed to provide an accurate estimation at 5 MHz, which is
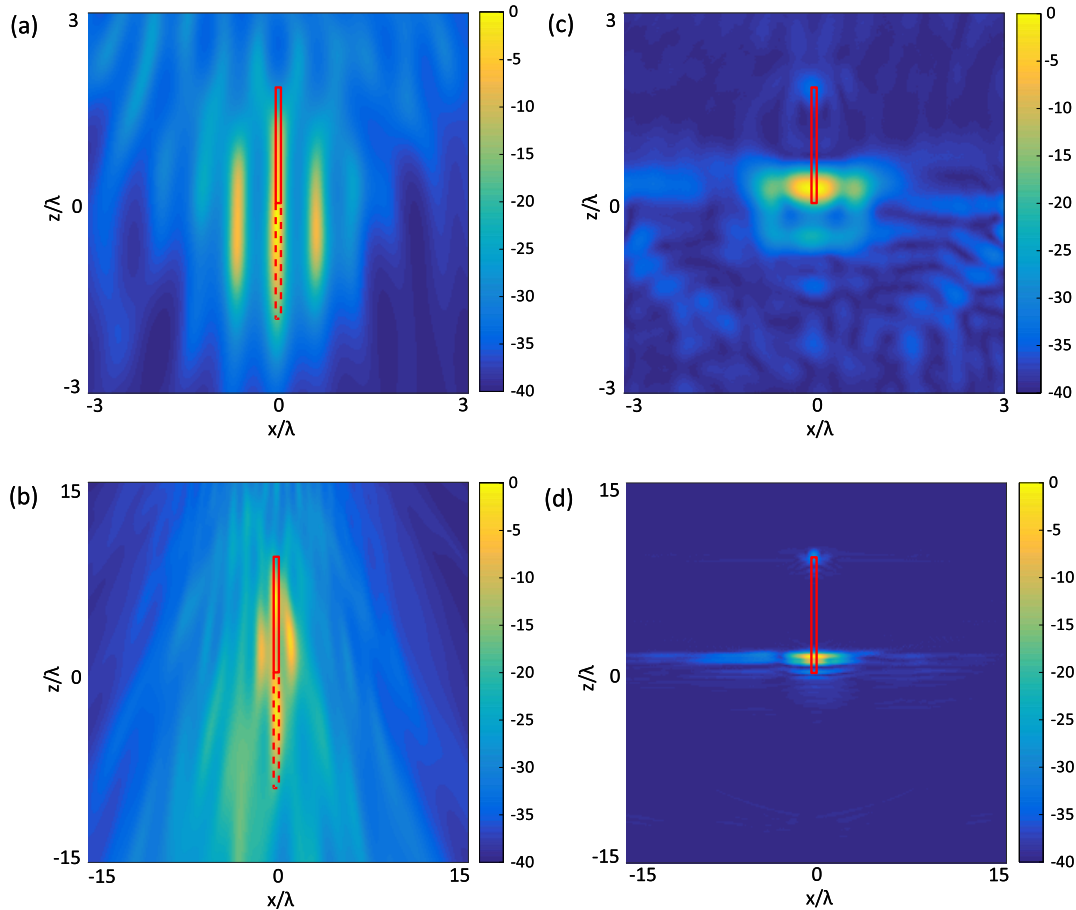
Fig. 14. Imaging results of the TFM and the FM based on the experiment data acquired by two different array probes. (a) FM image with a 1-MHz center frequency. (b) FM image with a 5-MHz center frequency. (c) TFM image with a 1-MHz center frequency. (d) TFM image with a 5-MHz center frequency. Note that the EDM notch is labeled in the images. The results here were from the experimental data.

TABLE II
FM AND TFM SIZING RESULTS BASED ON THE EXPERIMENT DATA—THE
TRUE CRACK SIZE IS 11 mm

|  | 1MHz probe | 5MHz probe |
|---|---|---|
| FM algorithm | 13.7mm | 36.4mm |
| TFM algorithm | 10.0mm | 9.7mm |

because for the 5-MHz probe, the small crack assumption of the FMC subtraction is not valid. These sizing results, based on the FM images, showed a very good consistency with the simulation results. The TFM provides us an accurate estimation of the crack depth at both 1 and 5 MHz. However, for the TFM image with a center frequency of 1 MHz, the implementation of the sizing needs the prior knowledge about the type of the defect, as the tip indication is easily to be masked by the artifacts. In addition, the FM overestimated the crack depth, while the TFM underestimated the crack depth.

## VI. CONCLUSION

Previous work on the FM for NDE was mainly concerned with the super-resolution effect [13], [18], [19], [35], but rarely addressed specific applications. This paper investigated the application of the FM algorithm on the subsurface imaging of the surface-breaking cracks. To evaluate the performance of the FM algorithm directly, the widely used imaging algorithm, the TFM algorithm, was used as a reference. The main challenge of this application of the FM algorithm is that the backwall will introduce a strong reflection which will mask the presence of the crack while imaging. In this paper, we developed a method to remove the backwall reflection before the imaging algorithm is applied, called "FMC subtraction" in this paper.

First, the TFM algorithm and the FM algorithm were applied to the simulated data and their performance were compared under different values of crack depth and noise level. Through the comparison, we found that the FM algorithm is able to correctly detect and accurately size a crack whose depth is not smaller than $1\lambda$, while the smallest crack that the TFM can be applied to s $2\lambda$. Additionally, the FM algorithm also gives good noise robustness as the FM algorithm is able to provide a sharp indication of the crack and an accurate sizing result under a high noise level (SNR = 5 dB). Then, the effects of the FMC subtraction were also studied through simulation. Through all the imaging and sizing results, the best performance of the FMC subtraction can be achieved when the crack depth is between $1\lambda$ and $3\lambda$. After all the simulation study, the FM algorithm and the FMC subtraction were applied to

experimental data. The results showed a good consistency with the simulations. From this, we found that the FM algorithm is able to image and size small surface-breaking cracks.

This paper also verifies the possibility of the FM as an alternative to the TFM for phased array imaging. This paper is to our mind a significant step toward the application of the FM to an experimental phased array imaging system. To achieve this goal completely, more work is required to explore the effect of different crack types, e.g., tilted cracks and true flaws.

## Acknowledgment

## References

[1] D. E. Bray and R. K. Stanley, *Nondestructive Evaluation: A Tool in Design, Manufacturing and Service*. New York, NY, USA: Taylor & Francis, 1996.

[2] S. Wilkinson and S. M. Duke, "Comparative testing of radiographic testing, ultrasonic testing and phased array advanced ultrasonic testing non destructive testing techniques in accordance with the AWS D1.5 bridge welding code," Dept. Mech. Eng., Univ. South Florida, Tampa, FL, USA, Tech. Rep. BDK84-977-26, Feb. 2014.

[3] V. Panchal, "Pumps and valves: NDT flaw detection," *World Pumps*, vol. 2014, no. 5, pp. 34–40, 2014.

[4] C. Hellier, *Handbook of Nondestructive Evaluation* (Mechanical Engineering), 2nd ed. New York, NY, USA: McGraw-Hill, 2012.

[5] N. Jain, "Replacement of radiography by phased array ultrasonic testing drives global ultrasonic NDT equipment market: Evolution of portable phased array ultrasonic testing equipment leads to large-scale uptake," *Quality*, vol. 53, no. 2, pp. 10–12, 2014.

[6] S.-C. Her and S.-T. Lin, "Non-destructive evaluation of depth of surface cracks using ultrasonic frequency analysis," *Sensors*, vol. 14, no. 9, pp. 17146–17158, 2014.

[7] S.-C. Her and S.-T. Lin, "Sizing detection of a surface-breaking crack by ultrasonic technique," in *Advances in Mechanical Engineering* (Applied Mechanics and Materials), vol. 52. Zurich, Switzerland: Trans Tech Publications, 2011, pp. 865–868.

[8] S. Baby, T. Balasubramanian, R. J. Pardikar, M. Palaniappan, and R. Subbaratnam, "Time-of-flight diffraction (TOFD) technique for accurate sizing of cracks embedded in sub-cladding," *Insight-Non-Destructive Test. Condition Monitor.*, vol. 45, no. 9, pp. 600–604, 2003.

[9] J. Zhang, B. W. Drinkwater, and P. D. Wilcox, "The use of ultrasonic arrays to characterize crack-like defects," *J. Nondestruct. Eval.*, vol. 29, no. 4, pp. 222–232, Dec. 2010.

[10] C. Holmes, B. W. Drinkwater, and P. D. Wilcox, "Post-processing of the full matrix of ultrasonic transmit–receive array data for non-destructive evaluation," *NDT E Int.*, vol. 38, no. 8, pp. 701–711, 2005.

[11] M. V. Felice, A. Velichko, P. D. Wilcox, and C. J. L. Lane, "Depth measurement of small surface-breaking cracks using the half-skip total focusing method," in *Proc. AIP Conf.*, 2015, vol. 1650. no. 1, pp. 994–1000.

[12] M. V. Felice, A. Velichko, and P. D. Wilcox, "Accurate depth measurement of small surface-breaking cracks using an ultrasonic array postprocessing technique," *NDT E Int.*, vol. 68, pp. 105–112, Dec. 2014.

[13] F. Simonetti, "Multiple scattering: The key to unravel the subwavelength world from the far-field pattern of a scattered wave," *Phys. Rev. E, Stat. Phys. Plasmas Fluids Relat. Interdiscip. Top.*, vol. 73, p. 036619, Mar. 2006.

[14] A. Kirsch and N. Grinberg, *The Factorization Method for Inverse Problems* (Oxford Lecture Series in Mathe). Oxford, U.K.: Oxford Univ. Press, 2008.

[15] B. Gebauer, M. Hanke, and C. Schneider, "Sampling methods for low-frequency electromagnetic imaging," *Inverse Problems*, vol. 24, no. 1, p. 015007, 2008.

[16] A. Kirsch, "Factorization of the far-field operator for the inhomogeneous medium case and an application in inverse scattering theory," *Inverse Problems*, vol. 15, no. 2, p. 413, 1999.

[17] T. Arens and N. Grinberg, "A complete factorization method for scattering by periodic surfaces," *Computing*, vol. 75, no. 2, pp. 111–132, Aug. 2005.

[18] F. Simonetti, "Localization of pointlike scatterers in solids with subwavelength resolution," *Appl. Phys. Lett.*, vol. 89, no. 9, p. 094105, 2006.

[19] T. Hutt and F. Simonetti, "Experimental observation of super-resolution imaging in highly attenuative materials," *Proc. SPIE*, vol. 7968, pp. 79680X-1–79680X-8, Mar. 2011.

[20] L. E. Kinsler, A. R. Frey, A. B. Coppens, and J. V. Sanders, *Fundamentals of Acoustics*, vol. 1. Hoboken, NJ, USA: Wiley, 2000.

[21] F. Cakoni and D. Colton, "The linear sampling method for cracks," *Inverse Problems*, vol. 19, no. 2, p. 279, 2003.

[22] M. Brignone, J. Coyle, and M. Piana, "The use of the linear sampling method for obtaining super-resolution effects in born approximation," *J. Comput. Appl. Math.*, vol. 203, no. 1, pp. 145–158, 2007.

[23] O. Bondarenko and A. Kirsch, "The factorization method for inverse scattering by a penetrable anisotropic obstacle with conductive boundary condition," *Inverse Problems*, vol. 32, no. 10, p. 105011, 2016.

[24] J. Guo, G. Yan, J. Jin, and J. Hu, "The factorization method for cracks in inhomogeneous media," *Appl. Math.*, vol. 62, no. 5, pp. 509–533, Oct. 2017.

[25] K. M. M. Tant, A. J. Mulholland, and A. Gachagan, "Application of the factorisation method to limited aperture ultrasonic phased array data," *Acta Acustica United Acustica*, vol. 103, no. 6, pp. 954–966, 2017.

[26] A. Kirsch, "Characterization of the shape of a scattering obstacle using the spectral data of the far field operator," *Inverse Problems*, vol. 14, no. 6, p. 1489, 1998.

[27] C. Fioralba and C. David, "On the mathematical basis of the linear sampling method," *Georgian Math. J.*, vol. 10, no. 3, pp. 411–425, 2003.

[28] Q. Chen, H. Haddar, A. Lechleiter, and P. Monk, "A sampling method for inverse scattering in the time domain," *Inverse Problems*, vol. 26, no. 8, p. 085001, 2010.

[29] V. Baronian, L. Bourgeois, and A. Recoquillay, "Imaging an acoustic waveguide from surface data in the time domain," *Wave Motion*, vol. 66, pp. 68–87, Nov. 2016.

[30] N. Khaji and S. D. Manshadi, "Time domain linear sampling method for qualitative identification of buried cavities from elastodynamic overdetermined boundary data," *Comput. Struct.*, vol. 153, pp. 36–48, Jun. 2015.

[31] T. Hutt and F. Simonetti, "Reconstructing the shape of an object from its mirror image," *J. Appl. Phys.*, vol. 108, no. 6, p. 064909, 2010.

[32] M. Smith, *ABAQUS/Standard User's Manual, Version 6.9*, SIMULIA, Providence, RI, USA, 2009.

[33] M. B. Drozdz, *Efficient Finite Element Modelling of Ultrasound Waves in Elastic Media*. London, U.K.: Univ. of London, 2008.

[34] P. Rajagopal, M. Drozdz, E. A. Skelton, M. J. S. Lowe, and R. V. Craster, "On the use of absorbing layers to simulate the propagation of elastic waves in unbounded isotropic media using commercially available finite element packages," *NDT E Int.*, vol. 51, pp. 30–40, Oct. 2012.

[35] F. Simonetti, L. Huang, N. Duric, and O. Rama, "Imaging beyond the born approximation: An experimental investigation with an ultrasonic ring array," *Phys. Rev. E, Stat. Phys. Plasmas Fluids Relat. Interdiscip. Top.*, vol. 76, p. 036601, Sep. 2007.
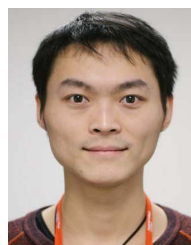
**Chao Zhang** received the B.Sc. degree in aircraft designing and engineering from Xi'an Jiaotong University, Xi'an, China, and the M.Sc. degree in advanced mechanical engineering from Imperial College London, London, U.K., where he is currently pursuing the Ph.D. degree.

He is currently a Research Assistant with the Non-Destructive Evaluation Group, Mechanical Engineering Department, Imperial College London. His current research interests include the use of ultrasonic phased array for nondestructive evaluation (NDE) and the development of super-resolution image reconstruction algorithms, with the application in NDE for small-size defect detection.

**Peter Huthwaite** received the M.Eng. and Ph.D. degrees in mechanical engineering from Imperial College London, London, U.K.

In 2016, he was a Lecturer in mechanical engineering with Imperial College London, where he leads imaging research and has undertaken extensive work on improving imaging algorithms, particularly for guided wave tomography with the Non-Destructive Testing Group. His main research area is limited data imaging for ultrasonics and radiography, to reduce issues associated with acquisition time, system complexity, and physical restrictions that occur in practice. His interests include the development of quantitative image reconstruction algorithms, with applications in medicine for breast cancer diagnosis and nondestructive testing for early stage damage detection, as well as the numerical modeling of waves, and GPU-based finite-element software package Pogo.



**Michael Lowe** received the B.Sc. degree in civil engineering from the University of Edinburgh, Edinburgh, U.K., and the M.Sc. and Ph.D. degrees in mechanical engineering from Imperial College London, London, U.K.

He worked in engineering consultancy from 1979 to 1989, specializing in the application and development of numerical methods for the solution of problems in solid mechanics. His principal clients were in the nuclear power and offshore oil industries. Since 1989, he has been with the Department of Mechanical Engineering, Imperial College London, where he is currently a Professor of mechanical engineering. He has authored over 250 journal and conference papers relating to ultrasound, guided waves, numerical modeling, and nondestructive evaluation (NDE). His current research interests include the use of ultrasound for NDE, with special interests in guided waves, the interaction of waves with defects and structural features, and numerical modeling.

Prof. Lowe was an Elected Fellow of the Royal Academy of Engineering in 2014 for his research contributions to NDE.